Thermal Science and Engineering (2022) Volume 5 Issue 1
doi:10.24294/tes.v5i1.1523

ORIGINAL RESEARCH ARTICLE

Numerical simulation and experimental study of contact thermal resistance under high temperature conditions

Linquan Shi, Qiang Li*
Nanjing University of Science and Technology, Nanjing 210094, Jiangsu province, China. E-mail: liqiang@njust.edu.cn

ABSTRACT

Contact thermal resistance is an important indicator of the efficiency of heat transfer between contact interfaces. The contact thermal resistance between the interfaces of superalloy GH4169 in high temperature was investigated by using ANSYS. The real surface morphology of superalloy was obtained with optical microscope, and its surface model was reconstructed in ANSYS. Based on the theory of structural mechanics, the elastoplastic deformation of the microstructure of the contact interface is simulated, and analyzed and obtained the contact thermal resistance between contact interfaces. The effect of interface temperature on the radiative heat transfer between the contact interfaces was studied. At the same time, the impact of radiation heat transfer between contact interfaces in high temperature is considered. Finally, it was tested by using an experimental test device. The result show that the maximum deviation between the contact thermal resistance and the contact thermal resistance was 12.60%, and the contact thermal resistance between superalloy interfaces decreases with the increase of interface temperature and contact pressure; the contact interface temperature difference increases first and then decreases with the increase of interface temperature.

Keywords: High Temperature; Contact Thermal Resistance; Numerical Simulation; High Temperature Alloys

ARTICLE INFO

Received: 12 January 2022
Accepted: 15 February 2022
Available online: 27 February 2022

1. Introduction

High-temperature interface contact heat transfer phenomena are widely found in fields of aerospace, energy power, iron and steel metallurgy and chemical industry, in high-temperature equipment such as space vehicles, nuclear reactors, internal combustion engines and coal gasification reactors. The contact thermal resistance exists between the contact interfaces of these heat exchange devices, and the presence of contact thermal resistance hinders the heat transfer. Therefore, contact thermal resistance is an important thermal property parameter that is of great importance in the scientific fields of defense, energy and materials.

The main methods for obtaining contact thermal resistance are theoretical predictions, numerical simulations and experimental measurements[1,2]. For theoretical prediction, the main approach is to perform theoretical analysis by building multi-point contact models for rough contact surfaces. Greenwood[3] proposed a method to calculate the contact thermal resistance as the total effect of the thermal resistance of all contact points in parallel, which have an assumed surface height distribution at the interface. Cooper *et al.*[4] proposed a similar prediction method to extend the assumption of a single cylindrical contact to multiple contact points by obtaining the distribution of roughness from surface morphometry. Liu and Zhang[5] proposed a finite element model based on a multi-point contact model to predict the contact thermal re-

sistance under high temperature conditions. For numerical models, methods mainly are finite element methods, finite difference methods and lattice Boltzmann methods etc. Cui *et al.*[6] established a multi-scale joint numerical simulation. By combining the lattice Boltzmann method with the traditional finite difference method, the heat transfer between two rough surfaces is calculated. Fang *et al.*[7] predicted the contact thermal resistance of interfaces with different interstitial media and considering radiation effects by a spliced multi-block Boltzmann method. Gou *et al.*[8] and Dai *et al.*[8] proposed contact thermal resistance prediction models based on actual surface topography and analyzed the effect of contact pressure and temperature on contact thermal resistance respectively. Xian *et al.*[10] investigated the effect of synergistic interaction between heat conduction and near-field thermal radiation at the contact interface on the contact thermal resistance at room temperature. Yang *et al.*[11] investigated the interfacial thermal resistance between graphene and polymer materials using molecular dynamics methods. As for experimental measurements, the contact thermal resistance can be measured using high-precision instruments with the heat flux method[12,13]. A large number of studies have been conducted to analyze the contact thermal resistance, but most of the models are mainly for the medium and low temperature environments, thus ignoring the effect of radiative heat transfer from the contact gap on the interface heat transfer. In the high temperature case, it is clear that the radiative heat transfer at the interface cannot be neglected. Although the effect of radiation at the interface on the contact thermal resistance was considered[7,9], the estimates made assume the contact interface as a radiative heat transfer between two smooth planes, which is obviously different from the actual interface contact. Therefore, it cannot elucidate the actual thermal radiation effect on the whole heat transfer process.

The interface contact thermal resistance is influenced by various factors, such as temperature, contact pressure, surface topography, material properties, etc., and the mechanical and thermal properties of the material change significantly at high temperatures compared to room temperature, so the study of the interface contact thermal resistance at high temperatures is particularly important. In this paper, we constructed a realistic micro-morphological model of the contact interface for the high temperature alloy GH4169, analyzed the heat transfer process (thermal conductivity, radiation) at the contact interface, and numerically simulated the contact mechanical process and heat transfer process at the contact interface of the superalloy by ANSYS to obtain the contact thermal resistance. Finally, the accuracy of the theoretical model was verified by conducting experimental tests using a high temperature contact thermal resistance test device.

2. Numerical simulation of contact thermal resistance

2.1 Calculation model

The high temperature alloy GH4169 is commonly used in high temperature environments such as aerospace and nuclear reactors. Some of the physical parameters of this material are shown in **Table 1**. Due to the wide range of temperature variations studied in this paper, the material's physical parameters are defined to be temperature dependent. In order to accurately simulate the contact of the high temperature alloy interface, the 3D model data for the numerical simulation in this paper are created with the morphological parameters of the actual rough surface. The three-dimensional surface morphology of the two rough contact surfaces of the high-temperature alloy was measured separately with a scanning laser confocal microscope model OLS-4100. The coordinate height matrix $z = z(x, y)$ of the surface profile was obtained by scanning the surface, where the scanning spacing in the x-direction and y-direction was $\Delta x = \Delta y = 10$ μm. Then the coordinate point matrix data is imported into ANSYS using the APDL command stream in ANSYS software, and through its bottom-up modeling process, the points, lines, surfaces, bodies are generated step by step to construct the numerical computation model shown in **Figure 1**, which has the dimensions of 1,000 μm × 1,000 μm × 2,010 μm. The surface roughness of the two contact interfaces are 1.26 and 1.18 μm respectively.

Table 1. Physical parameters of superalloy GH4169[14]

Temperature *t*/°C	Thermal conductivity λ/(W·m^{-1}·K^{-1})	Modulus of elasticity *E*/GPa	Poisson's ratio *μ*
20	13.4	205	0.30
100	14.7	201	0.30
200	15.9	193	0.30
300	17.8	187	0.30
400	18.3	181	0.31
500	19.6	175	0.32
600	21.2	168	0.32
700	22.8	160	0.33
800	23.6	151	0.33
900	27.6	141	0.34
1,000	30.4	129	0.34

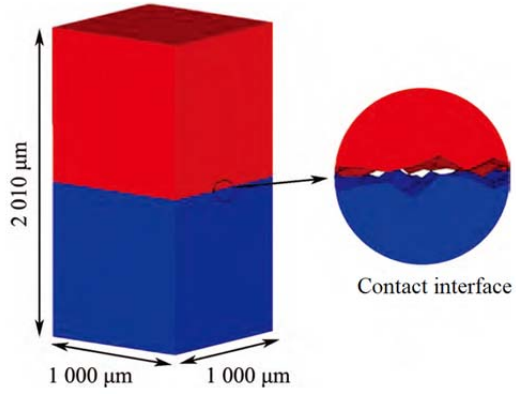

Figure 1. Numericalcalculationmodel.

2.2 Numerical methods and boundary conditions

2.2.1 Mechanical control equations

(1) Elastic stress—strain equation[15]

For an elastomer, the stress-strain in the elastic phase follows the equation of Hooke's law:

$$\mathrm{d}\sigma_i = D_{ij}^{\mathrm{e}}\,\mathrm{d}\varepsilon^{\mathrm{e}} \tag{1}$$

Where: $\sigma_i = (i = x, y, z)$ is the positive stress, D_{ij}^{e} is the elastic strain matrix, ε^{e} is the elastic strain. For isotropic materials equation (1) can be extended as:

$$\begin{bmatrix}\sigma_x\\ \sigma_y\\ \sigma_z\\ \tau_{xy}\\ \tau_{xz}\\ \tau_{yz}\end{bmatrix} = \frac{E}{1+\nu}\begin{bmatrix} m & n & n & 0 & 0 & 0\\ n & m & n & 0 & 0 & 0\\ n & n & m & 0 & 0 & 0\\ 0 & 0 & 0 & 1/2 & 0 & 0\\ 0 & 0 & 0 & 0 & 1/2 & 0\\ 0 & 0 & 0 & 0 & 0 & 1/2\end{bmatrix}\begin{bmatrix}\varepsilon_x\\ \varepsilon_y\\ \varepsilon_z\\ \gamma_{xy}\\ \gamma_{xz}\\ \gamma_{yz}\end{bmatrix} \tag{2}$$

Where: $m = \frac{1-\nu}{1-2\nu}$, $n = \frac{\nu}{1-2\nu}$; τ_{ij} is the shear stress; E is the modulus of elasticity; ν is the Poisson's ratio; γ_{ij} is the shear strain.

(2) Plastic stress—strain equation[15]

The classical metal plasticity model is used to solve the plastic deformation problem. Where the mechanical strain is decomposed into an elastic part and a plastic (inelastic) part, and the equation is:

$$\mathrm{d}\varepsilon_{ij} = \mathrm{d}\varepsilon_{ij}^{\mathrm{p}} + \mathrm{d}\varepsilon_{ij}^{\mathrm{e}} \tag{3}$$

Where: ε_{ij} is the total mechanical strain, ε_{ij}^{p} is the plastic strain, and ε_{ij}^{e} is the elastic strain. For metallic materials in the plastic strain phase it follows the generalized Hooke's law. Thus the relationship between the stress increment and the strain is:

$$\mathrm{d}\sigma_{ij} = D_{ij}^{\mathrm{ep}}\,\mathrm{d}\varepsilon \tag{4}$$

$$D_{ij}^{\mathrm{ep}} = D_{ij}^{\mathrm{e}} - D_{ij}^{\mathrm{p}} \tag{4}$$

Where: D_{ij}^{ep} is the elastic-plastic strain matrix; D_{ij}^{p} is the plastic strain matrix, which can be expressed by equation (6):

$$D^{\mathrm{p}} = \frac{9G^2 SS^{\mathrm{T}}}{\sigma_{\mathrm{s}}^2 (3G + E_{\mathrm{p}})} \tag{5}$$

Where: E_{p} is the plastic modulus, $E_{\mathrm{p}} = \frac{EE_t}{E-E_t}$, $E_t = \frac{\mathrm{d}\sigma}{\mathrm{d}\varepsilon}$, E_t is the slope of the stress-strain curve in the plastic phase; σ_{s} is the elastic-plastic stress; G is the shear modulus; S is the deflective stress tensor can be expressed by equation (7):

$$S = \begin{bmatrix} s_x & s_y & s_z & \tau_{xy} & \tau_{yz} & \tau_{zx}\end{bmatrix}^{\mathrm{T}} \tag{6}$$

$$s_i = \sigma_i - \frac{1}{3}(\sigma_x + \sigma_y + \sigma_z),\ (i = x, y, z) \tag{7}$$

2.2.2 Heat transfer control equations

(1) Heat conduction control equation[16]

$$\frac{\partial}{\partial x}\left(\lambda \frac{\partial T}{\partial x}\right)+\frac{\partial}{\partial y}\left(\lambda \frac{\partial T}{\partial y}\right)+\frac{\partial}{\partial z}\left(\lambda \frac{\partial T}{\partial z}\right)+\ddot{q}=\rho c \frac{\partial T}{\partial \tau} \tag{8}$$

Where: ρ and c are the density and specific heat capacity of the material respectively; $\ddot{q}$ is the internal heat source; λ is the thermal conductivity of the material, and its a function of temperature. In the model studied in this paper is a steady-state model without internal heat source, so for the internal heat conduction of the material the controlling equation is:

$$\frac{\partial}{\partial x}\left(\lambda \frac{\partial T}{\partial x}\right)+\frac{\partial}{\partial y}\left(\lambda \frac{\partial T}{\partial y}\right)+\frac{\partial}{\partial z}\left(\lambda \frac{\partial T}{\partial z}\right)=0 \tag{9}$$

(2) Heat transfer at the contact interface

Usually, the incomplete contact at the contact interface will form a contact gap, which is filled with air or other media, and therefore it will affect the heat transfer through the contact gap. Since the test sample is under high vacuum in this paper, the effect of gas heat transfer in the contact gap can be ignored. The heat transfer process at the contact interface is shown in **Figure 2**, where the heat is transferred by heat conduction at the contact point and by heat radiation at the contact gap.

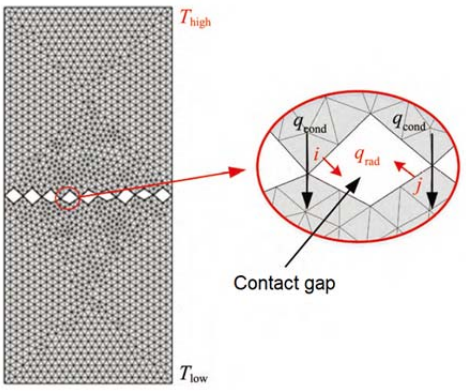

Figure 2. Schematic diagram of heat transfer at the contact interface.

The energy control equation at the contact interface is

$$\frac{\partial}{\partial x}\left(\lambda \frac{\partial T}{\partial x}\right)+\frac{\partial}{\partial y}\left(\lambda \frac{\partial T}{\partial y}\right)+\frac{\partial}{\partial z}\left(\lambda \frac{\partial T}{\partial z}\right)+q_{\text{rad}}=0 \tag{10}$$

Where, q_{rad} is the radiative heat transfer through the contact interface. In this paper, we use the light energy transfer solver in ANSYS software to model the radiation and thus solve the radiative heat transfer between the surfaces[17]. The radiant energy absorbed by surface i is

$$A_i q_{\text{in},i}=\sum_{j=1}^{N} A_j q_{\text{out},j} F_{ji} \tag{11}$$

Where: A_i is the area of surface i, $q_{\text{in},i}$ is the radiant heat flux absorbed per unit area of surface i, A_j is the area of surface j, $q_{\text{out},j}$ is the radiant heat flux per unit area of surface j, F_{ji} is the angular coefficient from the surface j to the surface i, N is the number of radiating surfaces in the contact gap. From the reciprocal relation of the angular coefficients it follows that:

$$A_j F_{ji}=A_i F_{ij}\ (j=1,2,3,\cdots,N) \tag{12}$$

Substituting equation (13) into equation (12) yields the radiant heat flux absorbed per unit area of surface i:

$$q_{\text{in},i}=\sum_{j=1}^{N} F_{ij} q_{\text{out},i} \tag{13}$$

Surface i radiant heat flow to the outside:

$$q_{\text{out},i}=\varepsilon_i \sigma T_i^4+\rho_i q_{\text{in},i}=\varepsilon_i \sigma T_i^4+(1-\varepsilon_i)\sum_{j=1}^{N} F_{ij} q_{\text{out},j} \tag{14}$$

Where: $q_{\text{out},i}$ is the radiant heat flux radiated outward from the surface i, ε_i and ρ_i are the emissivity and reflectivity of surface i, σ is Stephan-Boltzmann constant. Organizing equation (15) yields

$$\sum_{j=1}^{N}\left[\delta_{ij}-(1-\varepsilon_i)F_{ij}\right]q_{\text{out},j}=\varepsilon_i \sigma T_i^4$$

$$\begin{cases}\delta_{ij}=1 & \text{when } j=i\\ \delta_{ij}=0 & \text{when } j\neq i\end{cases} \tag{15}$$

Therefore, a series of linear equations can be constructed by equation (16) to calculate the radiant heat flux of each surface, and equation (16) can be written as

$$\left[A_{ij}\right]\left\{q_{\text{out},j}\right\}=\left\{E_i\right\} \tag{16}$$

Where: $A_{ij} = \delta_{ij} - (1-\varepsilon_i)F_{ij}$, $E_i = \varepsilon_i \sigma T_i^4$. Since the radiative heat transfer is related to the temperature of the temperature surface, it is necessary to solve the thermal radiation matrix (equation (17)) iteratively. By solving the heat radiation matrix, the radiant heat flux outward from each surface can be obtained $q_{\text{out},j}$. That is, the net radiant heat exchange for any one surface can be calculated $q_{\text{rad},i}$:

$$q_{\text{rad},i} = q_{\text{out},i} - q_{\text{in},i} = q_{\text{out},i} - \sum_{j=1}^{N} F_{ij} q_{\text{out},j} \tag{17}$$

2.2.3 Boundary conditions

In this paper, the static contact mechanics analysis and heat transfer analysis of the high temperature alloy contact interface are performed using ANSYS finite element software. The contact thermal resistance between interfaces is calculated with equation (19):

$$R = \frac{\Delta T_c}{q} = \frac{T_{\text{high}} - T_{\text{low}}}{q} \tag{18}$$

Where: R is the contact thermal resistance, ΔT_c is the temperature difference between high and low temperature interfaces, q is the average heat flow through the contact interface, T_{high} and T_{low} are the arithmetic mean temperatures of the high and low temperature interfaces respectively.

The boundary conditions for the mechanical analysis and heat transfer calculation are shown in **Figure 3**. In order to simulate the variation of the contact interface of the high-temperature alloy under different pressures, it is therefore necessary to impose corresponding fixed constraints on the model. Displacement constraints $(u_x = u_y = 0)$ are applied to each surface around the upper and lower models in the x and y directions respectively, while displacement constraints $(u_x = u_y = u_z = 0)$ are applied to the lower surface of the lower model in the x, y, and z directions respectively, to ensure that the entire model has displacement degrees of freedom only in the z direction, and finally the corresponding pressure p is applied on the upper surface of the upper model.

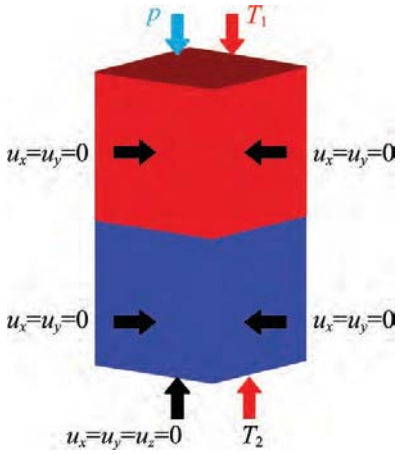

Figure 3. Boundary conditions.

Solving the contact deformation problem in ANSYS is highly nonlinear and requires an iterative solution. The structural mechanics units used in this numerical model are SOLID185 and SOLID186 units. The SOLID185 cell is an 8-node hexahedral mesh, which is a low-order cell and is used for general 3D model meshing. SOLID186 cell is a 20-node hexahedral mesh which is a high-order cell. It can be used for structures with irregular shapes, complex stress distribution or deformation, and can be used for the transition between hexahedral and tetrahedral meshes, so the SOLID186 cell is selected for meshing at the contact interface. The contact pairs are TARGE170 and CONTA174 cells, which can be used for 3D face-to-face contact. The contact pair contact detection in the contact interface is done with Gaussian integration method, and the contact algorithm is an extended Lagrangian method, which uses penalized updates of the iterative sequence. The contact stiffness is calculated automatically by the ANSYS solver based on the shape of the contact finite element.

In order to obtain the heat flux at the contact interface, a given constant temperature T_1, T_2 is applied to the upper surface of the upper model and the lower surface of the lower model respectively, so that the whole model has a certain temperature gradient, while each surface in the contact gap is set as a heat radiating surface and the remaining surrounding surfaces are adiabatic.

3. Experimental study of contact thermal resistance

3.1 Experimental test system

In order to verify the accuracy of the numerical simulation, a test device was used to measure the real contact thermal resistance of the high temperature alloy contact pair in vacuum. The system and test method for the experimental measurements were adopted[13] for the high temperature contact thermal resistance test system.

The system diagram of the test is shown in **Figure 4**, which mainly includes: pressure loading device, circulation cooling system, vacuum system, data acquisition system, high temperature heater, high temperature thermal shield. In order to avoid measurement errors caused by gas convection inside the chamber, the entire test chamber is under high vacuum (vacuum less than 10^{-3} Pa) due to the many factors affecting the contact thermal resistance. The high vacuum environment also prevents the oxidation of the test sample at high temperature, which may generate an oxide film at the interface and affect the test results.

Figure 4. Test test system and high temperature vacuum test chamber internal diagram.

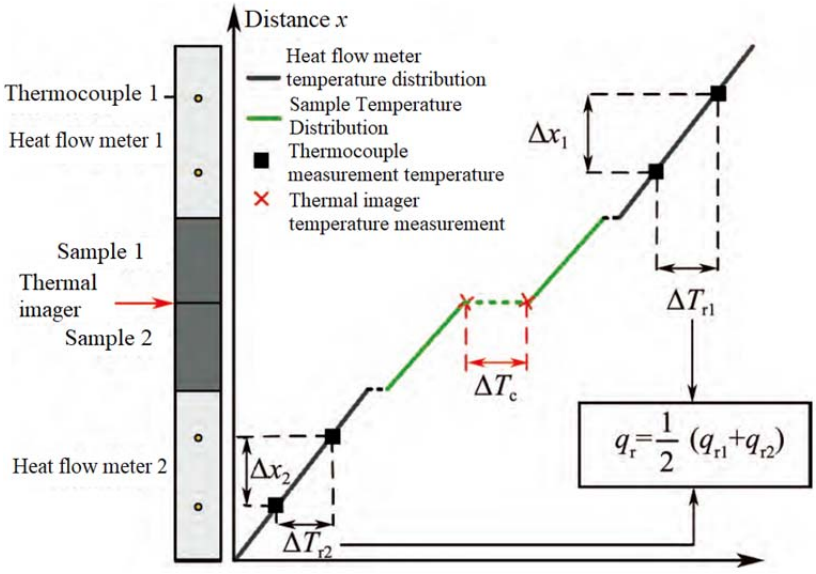

Figure 5. Schematic diagram of measurement of high temperature thermal contact resistance.

3.2 Experimental measurement principle

The measurement principle of the test system is based on the one-dimensional steady-state method, and the measurement principle is shown in **Figure 5**. According to the definition of the thermal resistance equation, the contact thermal resistance of the contact interface is

$$R = \frac{\Delta T_c}{q_r} \tag{19}$$

Where: R is the contact thermal resistance,

ΔT_c the contact interface temperature difference, q_r is the heat flow through the contact interface. Where the contact interface temperature difference ΔT_c is measured by an infrared thermal imaging camera, which observes the contact interface of the high temperature alloy by opening a sapphire window in the vacuum chamber. Heat flow q_r is measured by using a standard tungsten material heat flow meter. From the one-dimensional thermal conductivity Fourier equation:

$$q_r = -\lambda_r \cdot \frac{dT_r}{dx} \tag{20}$$

Where: q_r is the heat flow through the heat flow meter, λ_r is the thermal conductivity of the heat flow meter, dT_r/dx is the temperature gradient over the heat flow meter.

According to the measurement principle, the main factors affecting the accuracy of the contact thermal resistance test are: the temperature difference at the contact interface ΔT_c, the measurement temperature on the heat flow meter T_r, the position of the thermocouple on the heat flow meter x_r, the thermal conductivity of the heat flow meter material λ_r, and the heat loss of the system q_{loss}. The errors are analyzed separately and the measurement errors of the measurement system can be obtained by the error transfer equation:

$$\frac{U_R}{R} = \sqrt{\frac{U_{\Delta T_c}^2}{\Delta T_c^2} + \frac{U_{\lambda_r}^2}{\lambda_r^2} + \frac{U_{\Delta T_r}^2}{\Delta T_r^2} + \frac{U_{\Delta x_r}^2}{\Delta x_r^2} + \left(\frac{q_{loss}}{q}\right)^2} \tag{21}$$

The errors in equation (22) are shown in **Table 2**, so the measurement error of the test system is less than 15%.

3.3 Experimental measurement error

Table 2. Distribution of errors[13]

Error items	Thermal conductivity error of heat flow meter $\left(\frac{U_{\lambda_r}}{\lambda_r}\right)$/%	Thermocouple temperature error $(U_{\Delta T_r}/\Delta T_r)$	Thermocouple position error $(U_{x_r}/\Delta x_r)$	Thermal imaging camera temperature error $(U_{\Delta T_c}/\Delta T_c)$	System heat loss error (q_{loss}/q)	Overall system error (U_R/R)
Design Relative Error	5.00	7.80	3.30	5.00	10.00	14.98

4. Results and discussion

4.1 Comparison of numerical simulations and experimental measurements

Numerical simulations and experimental measurements were carried out for the high temperature alloy GH4169 material at different temperatures and pressures. The results of numerical simulations and experimental measurements are shown in **Figure 6**, where the pressures are 0.1, 0.2, 0.4, 0.6 MPa, and the interface temperature is 100–1000 °C. The interface temperature is equal to the arithmetic mean temperature of the upper and lower contact interfaces. The relative error in **Figure 6** is defined as:

$$\frac{\text{Experimental Measurement} - \text{Numerical Simulation}}{\text{Experimental Measurement}} \times 100\%$$

From **Figure 6**, the contact thermal resistance calculated by numerical simulation is $2.12 \times 10^{-5} \sim 2.77 \times 10^{-4} m^2 \cdot K \cdot W^{-1}$, and the contact thermal resistance measured experimentally is $2.29 \times 10^{-5} \sim 3.03 \times 10^{-4} m^2 \cdot K \cdot W^{-1}$. The results of the numerical simulation and the experimental measurement data have basically the same trend, and the maximum relative error between them is 12.60%, which is smaller than the measurement error of the experimental measurement system (15.00%), so the results of the theoretical simulation are reliable. A comparison of **Figure 6** shows that the relative error between the two at the same pressure tends to increase with the increase of temperature. This is due to the fact that as the measurement temperature increases, the heat loss in the experimental test system increases at high temperature measurement conditions, resulting in a smaller actual measured heat flow rate, which leads to an increase in the error between the experimental measurement and the theoretical simulation. However, the maximum error between the two is still within the measurement error of the test system. Regarding the variation of heat loss in the experimental test, the relationship between the radiation heat loss and temperature was investigated[18], showing that the effect of radiation heat loss be-

comes more obvious as the temperature increases and that the use of a heat shield reduces the heat loss. At the same time, the relative error between the two tends to decrease gradually as the pressure increases. This is due to the fact that when the pressure increases, the influence of other factors on the contact thermal resistance is limited, making the pressure the main factor affecting the contact thermal resistance.

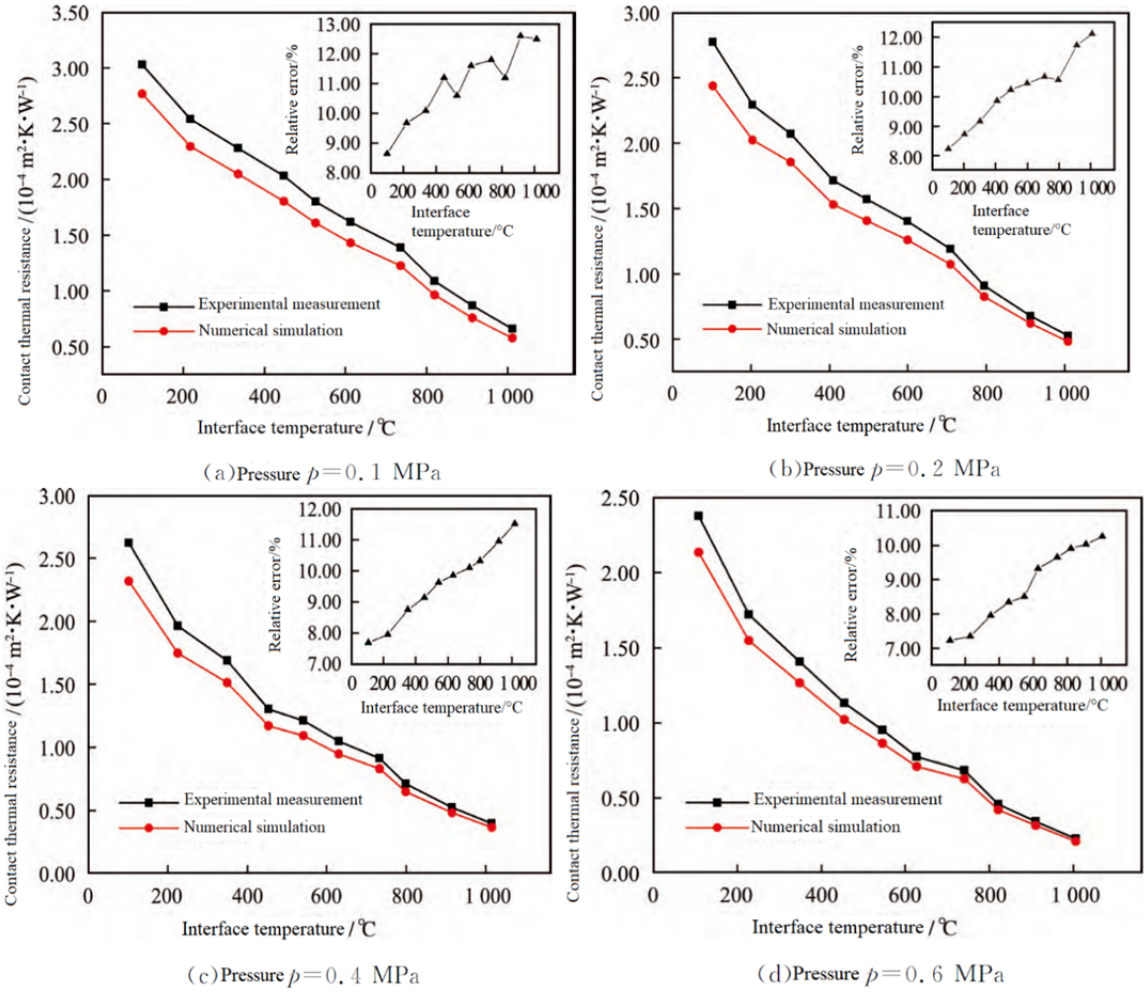

Figure 6. Numerical simulation and experimental measurement results.

4.2 Effect of interface temperature on high temperature contact thermal resistance

In this paper, we discuss the effect of interface temperature and contact pressure on contact thermal resistance. **Figure 7** shows the contact thermal resistance of the contact pair of high temperature alloy GH4169 at different interface temperatures and contact pressures.

As shown in **Figure 7**, the contact thermal resistance decreases with the increase of the contact interface temperature at the same pressure. There are two main reasons for this phenomenon. On the one hand, it is related to the temperature dependence of the material mechanical properties of the high temperature alloy. From **Table 1**, it can be found that the modulus of elasticity of high temperature alloy GH4169 decreases gradually with the increase of temperature, so that even at the same pressure, the increase of the interface temperature leads to a larger deformation of the contact point on the contact interface and thus generates more contact area, so that more heat can be transferred through the contact surface in the form of heat conduction, thus reducing the contact thermal resistance. **Figure 8** and **9** shows the variation of the actual contact area A_C with different temperatures. In **Figure 9**, A_C/A is the ratio of the actual contact area A_C to the nominal contact area A. It can be seen that the actual contact area increases as the interface temperature increases, and the tendency to

increase is accelerated at high temperatures.

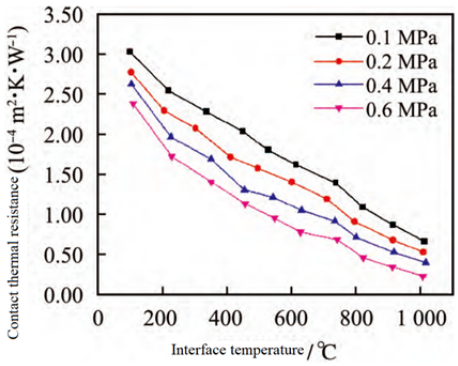

Figure 7. Influence of interface temperature and pressure on thermal contact resistance.

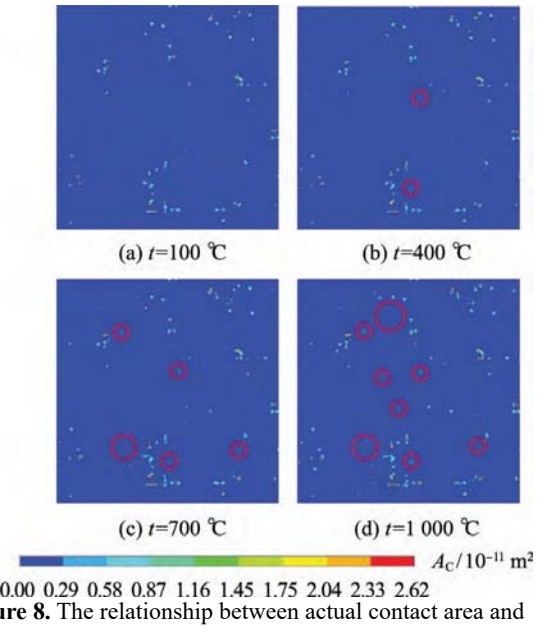

Figure 8. The relationship between actual contact area and temperature (p = 0.6 MPa).

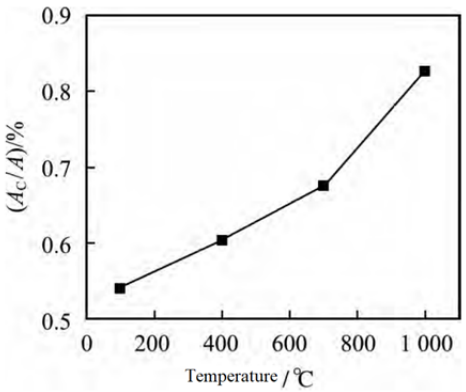

Figure 9. The percentage of actual contact area to nominal contact areavaries with temperature.

Another aspect of the effect of temperature on the thermal contact resistance is due to the increase in thermal conductivity of the high temperature alloy material due to the increase in temperature, as shown in **Table 1**, and it is related to the enhanced radiative heat transfer between the contact interfaces. **Figure 10** illustrates the variation of the proportion of radiative heat transfer at the contact interface in the total heat transfer with the change of interface temperature at pressure 0.6 MPa. It can be found that as the interface temperature increases, the proportion of radiative heat transfer to the total heat transfer gradually increases, which leads to an increase in the total heat transfer at the interface, resulting in a decrease in the interface temperature difference. **Figure 11** shows the variation of the contact interface temperature difference with the change of interface temperature. The interface temperature difference increases with the increase of the interface temperature when the temperature is 100–600 °C. When the interface temperature exceeds 700 °C, a turning point occurs, and the interface temperature difference decreases with the increase of the interface temperature. This is due to the fact that when the temperature is below 700 °C, the radiation heat transfer accounts for less than 10% of the heat transfer, and the radiation effect on the total heat transfer is not obvious at this time, so the interface temperature difference is gradually increasing. When the interface temperature exceeds 700 °C, the effect of radiation becomes more significant and the decrease in mechanical properties of the material analyzed earlier leads to an increase in the contact area, which in combination increases the total heat transfer at the interface, decreases the temperature difference at the contact interface, and decreases the contact thermal resistance.

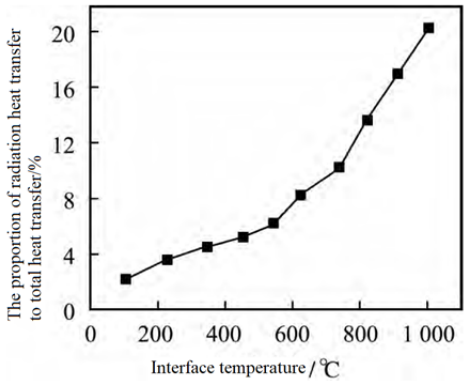

Figure 10. Variationtrend of radiation heat transfer with interface temperature.

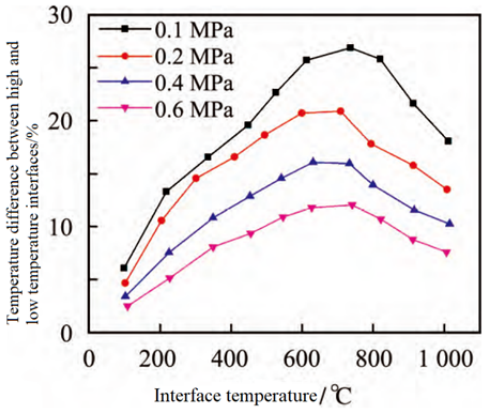

Figure 11. Interface temperature variation.

4.3 Effect of contact pressure on high temperature contact thermal resistance

As shown in **Figure 7**, the contact thermal resistance decreases with the increase of contact pressure at the same interface temperature. This phenomenon can be explained in terms of material mechanics. The deformation of the material, no matter elastic or plastic, is positively related to the pressure on the material, so that the deformation of the interface increases as the contact pressure increases, and thus the actual contact area increases. **Figure 12** shows the distribution of the actual contact area on the contact surface at different contact pressures, which clearly shows that the actual contact area increases as the contact pressure increases. **Figure 13** shows the variation of the ratio between the pressure and the actual contact area A_C and the nominal contact area A. It can be seen that the relationship is approximately linear, which is consistent with the findings of Carbone *et al.*[19].

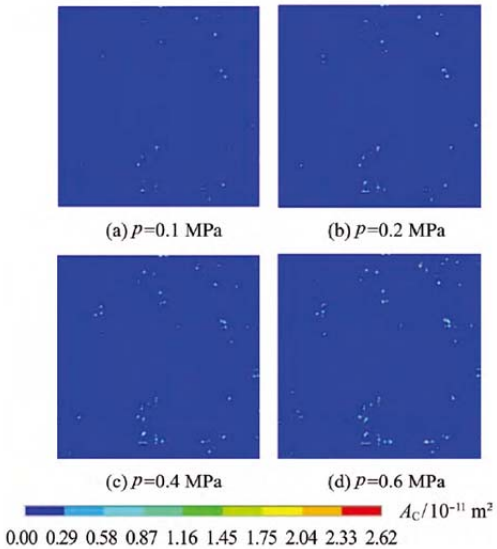

Figure 12. The relationship between actual contact area and pressure.

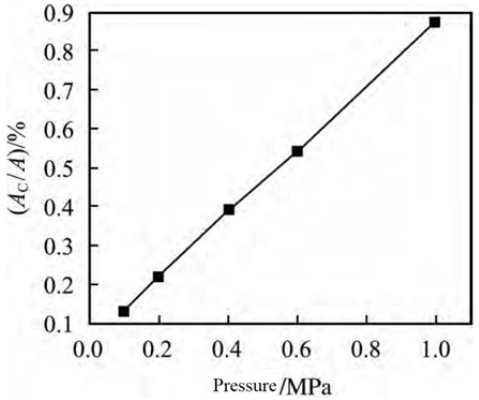

Figure 13. The percentage of actual contact area to nominal contact area varies with pressure.

5. Conclusion

(1) Based on the material of high temperature alloy GH4169, a numerical model of the mechanics and heat transfer at the contact interface under high temperature conditions was established and tested, and the numerical simulation results were nicely in agreement with the experimental test results, which proved the accuracy of the numerical model.

(2) The contact thermal resistance decreases with the increase of interface temperature under high temperature conditions. On the one hand, it is due to the decrease of the mechanical properties of the material caused by the increase of temperature, which leads to the increase of the actual contact area. On the other hand, the thermal conductivity of the studied materials increases with increasing temperature, while the thermal radiation effect at the contact interface is enhanced at high temperatures, which facilitates the heat transfer between the contact interfaces. The contact thermal resistance decreases with increasing contact pressure because higher pressure helps to increase the actual contact area and thus enhances the heat transfer between the contact interfaces.

(3) The temperature difference at the contact interface of a high temperature alloy increases with the increase of the interface temperature and then tends to decrease after reaching a certain temperature, which is worth noting for the design of high temperature thermal protection.

Conflict of interest

The authors declared that they have no conflict of interest.

References

1. Wang A, Zhao J. Review of prediction for thermal contact resistance. Science China Technological Sciences 2010; 53: 1798–1808.
2. Zhang P, Xuan Y, Li Q. Development on thermal contact resistance. CIESC Journal 2012; 63(2): 335–349.
3. Greenwood JA. Constriction resistance and the real area of contact. British Journal of Applied Physics 2002; 17(12): 1621–1632.
4. Cooper MG, Mikic BB, Yovanovich MM. Thermal contact conductance. International Journal of Heat and Mass Transfer 1969; 12(3): 279–300.
5. Liu D, Zhang J. Numerical simulation of high-temperature thermal contact resistance and its reduction mechanism. PLOS ONE 2018; 13(3): e194483.
6. Cui T, Li Q, Xuan Y, *et al*. Multiscale simulation of thermal contact resistance in electronic packaging. International Journal of Thermal Sciences 2014; 83: 16–24.
7. Fang W, Gou J, Chen L, *et al*. A multi-block lattice Boltzmann method for the thermal contact resistance at the interface of two solids. applied thermal engineering 2018; 138: 122–132.
8. Gou J, Ren X, Dai Y, *et al*. Study of thermal contact resistance of rough surfaces based on the practical topography. Computers & Fluids 2018; 164: 2–11.
9. Dai Y, Gou J, Ren X, *et al*. A test-validated prediction model of thermal contact resistance for Ti-6Al-4V alloy. Applied Energy 2018; 228: 1601–1617.
10. Xian Y, Zhang P, Zhai S, *et al*. Re-estimation of thermal contact resistance considering nearfield thermal radiation effect. Applied Thermal Engineering 2019; 157: 113601.
11. Yang B, Li M, Gao J, *et al*. Temperature dependence study on thermophysical properties of graphene foam and the correlation with interface thermal conductance. Journal of Thermal Science and Technology 2019; 18(4): 259–265.
12. Zhang P, Xuan Y, Li Q. A high-precision instrumentation of measuring thermal contact resistance using reversible heat flux. Experimental Thermal and Fluid Science 2014; 54: 204–211.
13. Xuan Y, Li Q, Zhang P. Measurement method and instrument of thermal contact resistance at high temperature. Scientia Sinica (Technologica) 2019; 49(5): 491–500.
14. China Aviation Materials Handbook Committee. Zhongguo hangkong cailiao shouce (Chinese) [China aviation materials handbook]. Beijing: China Standard Press; 2002.
15. Zhu B. Youxian danyuanfa yuanli yu yingyong (Chinese) [The finite element method theory and applications].4th ed. Beijing: China Water Power Press; 2018.
16. Yang S, Tao W. Chuanrexue (Chinese) [Heat Transfer]. 4th ed. Beijing: Higher Education Press; 2006.
17. Ling G. ANSYS 14.0 relixue fenxi cong rumen dao jingtong (Chinese) [ANSYS 14.0 thermodynamic analysis from entry to proficiency]. Beijing: Tsinghua University Press; 2013.
18. Madhusudana CV. Accuracy in thermal contact conductance experiments-the effect of heat losses to the surroundings. International Communications in Heat and Mass Transfer 2000; 27(6): 877–891.
19. Carbone G, Bottiglione F. Asperity contact theo-ries: Do they predict linearity between contact area and load? Journal of the Mechanics and Physics of Solids 2008; 56(8): 2555–2572.